

## IMPROVING THE TAGG'S SLOPE METHOD FOR LARGE-SCALE GROUNDING SYSTEMS THROUGH FINITE ELEMENT METHOD SIMULATIONS

Miguel Martínez-Lozano

Technical University of Madrid, School of Industrial Engineering, Department of automation, electrical and electronic engineering and industrial computing, Spain (✉ [miguel.mlozano@upm.es](mailto:miguel.mlozano@upm.es))

### Abstract

Measuring the grounding resistance of very large installations is difficult because conventional fall of potential methods require impractically long test leads. The Tagg Slope Method reduces this distance, but its traditional formulation neglects finite electrode dimensions and relies on curve extrapolations outside the range originally analyzed, leading to large errors.

This paper revises the method using finite element simulations that model realistic electrode geometry and soil conduction. A new relationship between voltage-profile slope and measuring-electrode position is obtained and fitted by a polynomial with errors below 0.02%. The corrected method is tested on large square grounding grids and on a photovoltaic-plant grounding system. Results show that, when measurements are taken away from corner regions and with auxiliary-electrode distances above about 20% of the system diagonal, the grounding resistance can be estimated with errors below 3%, while the traditional implementation may produce errors of several tens of percent.

Keywords: Grounding resistance measurement, Large grounding systems, renewable plants, Fall of Potential Method (FOPM), Tagg Slope Method (TSM), Finite Element Method (FEM)

### 1. Introduction

Grounding systems are essential for electrical safety and continue to be an active research area, particularly regarding soil resistivity, electrode design, and resistance verification [1–4]. However, conventional *Fall of Potential* (FOP) methods require large auxiliary-electrode spacings that are often impractical. In urban environments [4] and in large renewable facilities such as photovoltaic and wind plants [5], limited space and long test-lead lengths introduce inductive effects and large measurement errors. Although several alternative impedance-measurement techniques exist [6], most lack broad industrial acceptance without strong validation. As a result, accurately measuring grounding resistance in these scenarios remains challenging and motivates the revision of current methodologies [3].

This study focuses on the methodology proposed by Tagg [7, 8], adopted in IEEE Std 81 [1, 3] for measuring large grounding systems and commonly referred to as the *Tagg Slope Method* (TSM). This method enables grounding resistance measurements using the *Fall of Potential Method* (FoPM) but with *current electrode* (CE) distances shorter than those required by the conventional approach. The technique relies on obtaining a voltage profile using a distant CE and a *potential electrode* (PE), determining the slope  $\mu$  of this profile, and applying a correction to identify the theoretical PE position that yields the correct resistance measurement.

IEEE Std 81 [1] includes this approach in a dedicated section and provides a correction table (Table 5) for  $\mu$  values between 0.4 and 1.6, originally derived from Tagg's work [7, 8]. The draft of the upcoming IEEE revision [3] replaces this table with a fourth-order polynomial curve fit, extending only the upper limit ( $\mu < 2$ ). However, this curve fitting does not accurately

represent the theoretical behaviour in the range  $1.6 < \mu < 2$ , as it extrapolates from data within  $0.4 < \mu < 1.6$  without incorporating Tagg's original equation in the extended range.

Recent studies have highlighted inconsistencies in *TSM*, especially when  $\mu$  exceeds the IEEE tabulated range or when analytical assumptions depart from realistic electrode geometry [9–14]. These issues motivate a reevaluation of the method.

Furthermore, [14] introduces correction factors to account for deviations from the original methodology, demonstrating that the Tagg Slope Method still requires deeper examination. These findings highlight the need for a more robust theoretical foundation to better define its practical limitations.

Nonetheless, key issues remain. Tagg's original formulation imposes the constraint  $0.5714 < \mu < 2$ , which is not respected in the current IEEE range, and the simplification of modelling the CE as a point neglects the influence of its radius on the potential distribution.

In this work, these limitations are addressed through *finite element method* (FEM) simulations of hemispherical configurations, solving Poisson's equation under electrostatic conditions to account for soil conductivity. The simulations enable a re-evaluation and correction of Tagg's results, leading to an updated equation for determining the effective PE position as a function of  $\mu$ . The study further applies this analysis to some practical grounding configurations: a long square mesh and a *photovoltaics* (PV) plant. This work revises *TSM* using finite element simulations and evaluates its performance in large grounding systems.

## 2. Theoretical background

### 2.1. Measurement of Grounding Resistance Using the Tagg Slope Method

The *TSM* is a specific implementation of the *FoPM* [1, 7]. As shown in Fig. 1, a current  $I$  is injected into the electrode under test (E), and returned through the auxiliary current electrode CE, located at distance  $C$ . The PE is then moved along the  $y$ -axis to obtain  $R_m$ , defined as the voltage difference between E and PE divided by  $I$ . From the resulting potential distribution, the grounding resistance  $R_E$  of the electrode can be estimated.

From an analytical point of view [7, 8], Tagg modelled the electrode E as a hemisphere of radius  $r$ , with the auxiliary CE placed at a distance  $C$  and the PE at a distance  $P$ . When a current  $I$  is injected between E and CE, a potential is developed at electrode E given by (1), and an analogous potential appears at electrode PE, expressed [7]:

$$vE = \frac{\rho \cdot I}{2\pi} \cdot \left[ \frac{1}{r} - \frac{1}{C} \right], \quad (1)$$

$$vPE = \frac{\rho \cdot I}{2\pi} \cdot \left[ \frac{1}{P} - \frac{1}{C-P} \right]. \quad (2)$$

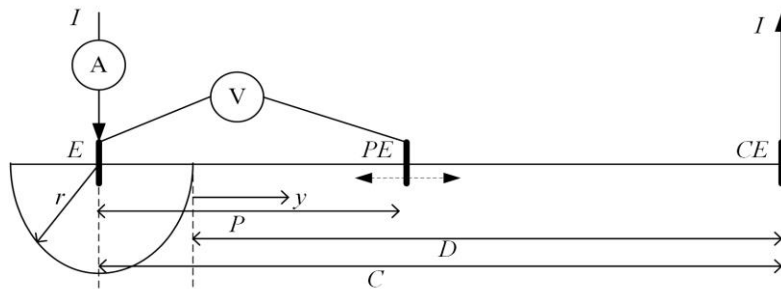


Fig. 1. Spatial scheme.

The potential difference between these two points, denoted  $V_m$ , is given by (3). Dividing this value by the current  $I$  result in the measured resistance  $R_m$ , expressed in (4), which is a function of the position  $P$  of the auxiliary potential electrode PE:

$$V_m = vE - vPE = \frac{\rho \cdot I}{2\pi} \cdot \left[ \frac{1}{r} - \frac{1}{C} - \frac{1}{P} - \frac{1}{C-P} \right], \quad (3)$$

$$R_m = \frac{V_m}{I} = \frac{\rho}{2\pi} \cdot \left[ \frac{1}{r} - \frac{1}{C} - \frac{1}{P} - \frac{1}{C-P} \right]. \quad (4)$$

As shown in Fig. 2, the potential-drop profile depends on the spacing  $C$  between the test electrode E and the auxiliary current electrode CE. Since both electrodes contribute to the measured potential, the FoPM requires  $C$  to be sufficiently large for their fields not to overlap [7]. When  $C \gg r$ , typically 5–10  $r$ , the potential profiles resemble the case C1 in Fig. 2, and  $R_E$  can be obtained from the  $R_m$  curve by placing the potential electrode at approximately 61.8% of  $C$  ( $K_1 = 0.618$ ). In contrast, for smaller separations such as C2 (and similarly C3) the potential profiles overlap significantly, preventing the direct application of the FoPM and making it necessary to use alternative techniques such as the TSM.

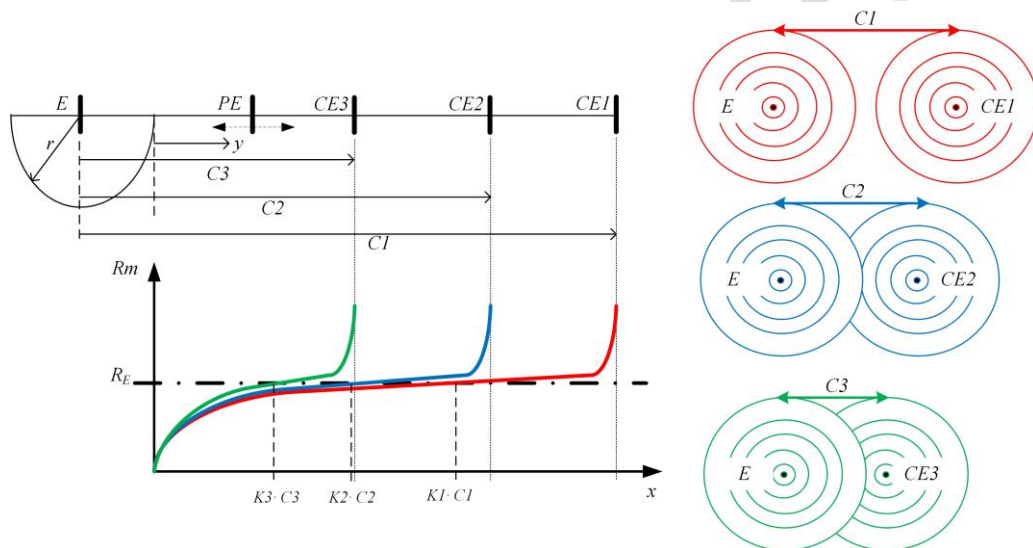


Fig. 2. Fall of potential method.

The slope method establishes the following procedure: for a distance  $C3$ , *p.e.*, three measurements of  $R_m$  are taken at different positions  $P$  of the PE electrode: the first at 0.2 times  $C3$  ( $R_{m1}$ ), the second at 0.4 ( $R_{m2}$ ) and the third at 0.6 ( $R_{m3}$ ). The relationship among these three points is [7] and [8] the slope  $\mu$  and is determined by

$$\mu = \frac{R_{m3} - R_{m2}}{R_{m2} - R_{m1}}. \quad (5)$$

Tagg derived a closed-form solution to (4) by using three points of the FoPM curve to obtain a quadratic expression that identifies the position at which the calculated resistance matches the theoretical value. He initially proposed using measurements at 0.4, 0.6, and 0.8  $C$  [7], later extending the range to 0.2–0.8  $C$  [8]. The approach adopted in IEEE standards [1–3], and followed in this work, uses the three measurements at 0.2, 0.4, and 0.6  $C$  to solve (4).

Once  $\mu$  is known, the corresponding  $PE$  position can be obtained from Tagg's solution to (4) [7, 8]. In (4), the first term gives the true grounding resistance  $R_E$ , while the remaining terms represent the measurement error. Using the three measured values  $R_{m1}$ ,  $R_{m2}$ , and  $R_{m3}$ , Tagg determined the  $PE$  location at which this error becomes zero. Because the result depends solely

on  $\mu$  for uniform soils, the IEEE standard [1] provides the corresponding PE positions in Table 5 of [1], summarized in Table 1 of this work.

Table 1. Some representative data from table 5 [1] establishing PE position for a value of  $m$ .

$\mu$	PE position*	$\mu$	PE position*
0.40	0.643	0.5	0.629
0.75	0.589	1	0.542
1.5	0.389	1.59	0.341

\*The PE position is in per unit of the current electrode position or distance (CE).

The updated IEEE 81 draft [3] introduces a curve-fitted expression derived directly from the tabulated values, given in (6). A similar curve-fitting approach is also presented in [10] and [11], whose corresponding expression:

$$P/C = -0.1357 \cdot \mu^4 + 0.4196 \cdot \mu^3 - 0.5395 \cdot \mu^2 + 0.1509 \cdot \mu + 0.646, \quad (6)$$

$$P/C = -0.1242 \cdot \mu^3 + 0.2339 \cdot \mu^2 - 0.3049 \cdot \mu + 0.738. \quad (7)$$

Where  $P/C$  is the ratio between the position at which the PE electrode must be placed and the distance to the CE electrode  $C$ . Neither [3] nor [10] report the correlation parameters or fitting errors associated with their curve-fitting procedures.

## 2.1. Considerations and Limitations

The TSM relies on simplified assumptions, including neglecting electrode dimensions, which introduces systematic errors at short electrode spacings. This motivates the need for a corrected formulation. Tagg's potential expression omits the radius of the hemispherical electrode [7], which is corrected:

$$vE = \frac{\rho \cdot I}{2\pi} \cdot \left[ \frac{1}{r} - \frac{1}{c-r} \right]. \quad (8)$$

The analytical model also neglects the radius of the auxiliary electrode  $r_{CE}$ , further reducing accuracy for small spacings. FEM simulations are therefore required to obtain corrected slope-method factors beyond those in Table 1 and expressions (6) and (7).

From (4), as illustrated in Fig 3a, the theoretical bounds are  $0.5714 < \mu < 2$ , yet IEEE 81 provides values only for  $0.4 < \mu < 1.6$ , creating inconsistencies with the method's analytical basis.

The curve-fitting formulas in [3, 10, 11], based solely on the IEEE table 5 dataset [1] (table 1), do not reproduce the analytical solution for  $\mu > 1.6$ , with deviations up to 60%.

As illustrated in Fig. 3b, the 'IEEE' data [1] span only  $0.4 < \mu < 1.6$ , while 'P81/D4' [3] corresponds to (6) and 'PUB' [10, 11] to (7), evaluated over  $0.6 < \mu < 1.9$ . The 'Analyt' set represents the exact solution of (4). Notice that the anomalous point in the IEEE curve [1] at  $\mu = 0.92$  results from a typographical error in the standard.

Using the analytical solution of (4), a complete  $\mu$  vs  $P/C$  dataset was generated and fitted with the fifth-order polynomial (9), achieving a correlation of 0.9996:

$$P/C = -0.9026 \cdot \mu^5 + 4.824 \cdot \mu^4 - 10.17 \cdot \mu^3 + 10.41 \cdot \mu^2 - 5.314 \cdot \mu + 1.696. \quad (9)$$

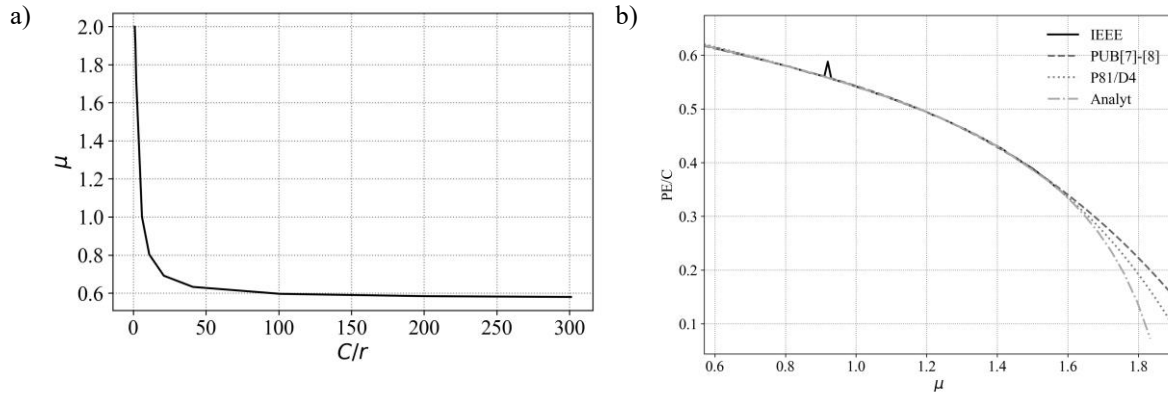


Fig. 3. Considerations about  $\mu$ : a) analytical limits of  $\mu$  and b) Differences in the curve fitting process.

The limitations of the TSM as defined in current standards justify the revised approach proposed here. The following methodology updates the  $P/C$  values using FEM simulations with hemispherical electrodes, preserving Tagg's original concept. The corrected  $P/C$  data are then applied to three case studies to validate their performance for large, complex grounding systems typical of utility-scale renewable plants.

### 3. Proposed methodology

This section derives the  $P/C-\mu$  relationship, determining the required PE position as a function of  $\mu$  following Tagg's original principles [7, 8], but using finite element simulations rather than simplified analytical formulas. The analysis employs *ANSYS Electronic Desktop 2025 R2*. Two hemispherical electrodes, E (radius  $r$ ) and CE (radius  $r_{CE}$ ), separated by distance  $C$  are modeled, and a 1 A current is injected between them to obtain the potential profile along the line joining their centers. The geometry and dimensions used are shown on Fig. 4.

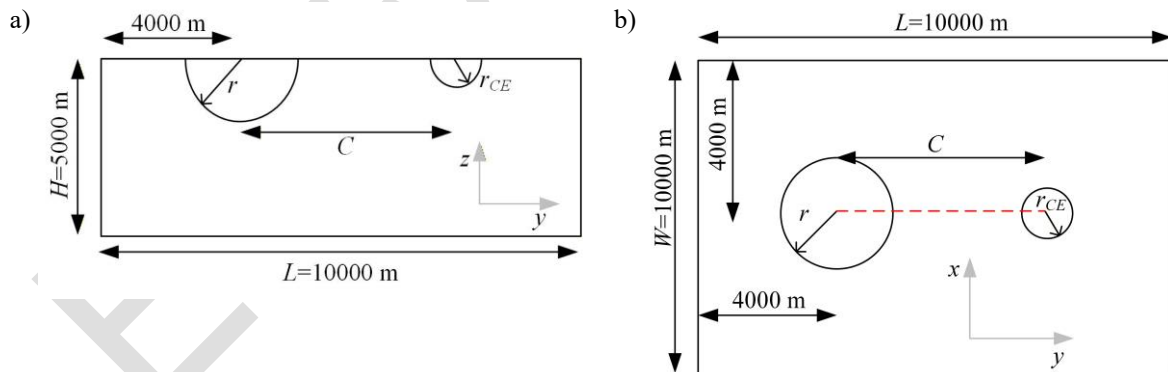


Fig. 4. Geometry used for the methodology: a) cross section and b) plan view.

The problem was solved using the finite element method [15, 16] with an electroquasistatic formulation to solve the small electric currents in a conductive media ( $\sigma, \rho = 1/\sigma$ ). The governing equation is the charge conservation law expressed by

$$\nabla \cdot (\sigma \nabla V + j\omega \epsilon \nabla V + J_e) = 0, \quad (10)$$

where  $V$  is the electric potential,  $\sigma$  the electrical conductivity,  $\epsilon$  the permittivity, and  $J_e$  an externally applied current density. The electric field is given by

$$E = -\nabla V, \quad (11)$$

and the total current density by

$$J = \sigma E + j\omega \epsilon E. \quad (12)$$

The model uses a prescribed current source and zero-potential (Dirichlet) conditions on the outer boundaries. The computational domain was sized ( $L = 10000$  m,  $W = 10000$  m,  $H = 5000$  m) to avoid boundary influence on the potential. The applied boundary conditions are shown in Fig. 5.

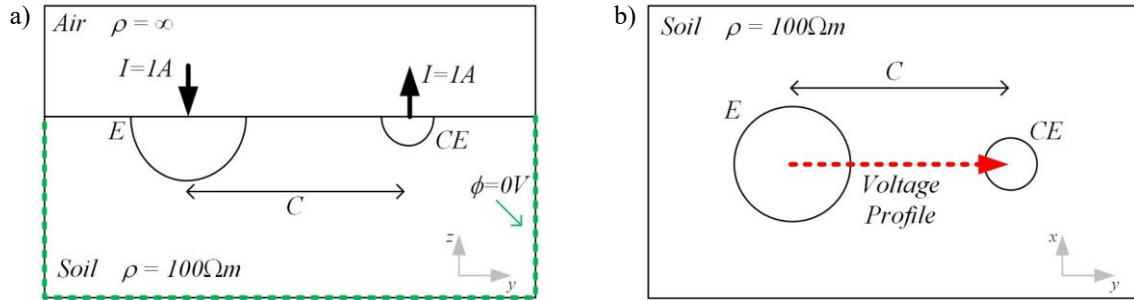


Fig. 5. Boundary conditions defined in the problem statement: a) cross section and b) plan view.

### 3.1. Scenarios considered

To obtain a general  $P/C$  vs  $\mu$  correlation, multiple simulation scenarios were defined considering the key parameters affecting the potential profile, as summarized in Table 2.

Table 2. Scenarios considered for the simulations.

Variable	Range
$r$ (radius of electrode E) [m]	{100, 200, 300 and 500}
$r_{CE}$ (radius of electrode CE) [m]	{0.1, 0.5, 1}
$C$ (distance between E and CE) [m]	{1.1, 1.2, 1.3, 1.4, 1.5, 1.6, 1.7, 1.8, 1.9, 2, 2.25, 2.5, 2.75, 3, 3.25, 3.5, 3.75, 4, 4.5, 5, 6, 7, 8, 9, 10, 10, 20} times $r$

All simulations used the same parameters: a 1 A injected current, uniform soil resistivity of  $100 \Omega \cdot m$ , the defined domain dimensions, and grounded external boundaries. A refined mesh ( $\sim 350,000$  nodes and 3 million DOF) was constructed to accommodate the geometric scale differences, following accepted FEM practices for electrical problems [17–19]. Additionally, a preliminary simulation without the CE electrode was performed to obtain the reference resistance  $R_{E,FEM}$  for each value of  $r$ .

### 3.2. Analysis of the scenarios considered

For each scenario, the potential profile along the  $y$ -axis was computed between the effective boundaries of electrodes E and CE, *i.e.*, from  $d = 0$  at the edge of E to  $d = C - (r + r_{CE})$  at the edge of CE, excluding the constant-potential regions. Potentials are positive near E (where current enters) and negative near CE (where it exits). To express the data in the form required for the FPM, the profile is shifted by adding  $U_E$  and inverted so that  $V_m = 0$  at  $d = 0$ , producing the corresponding  $R_m$  profile used in the analysis. The resulting transformation is illustrated in Fig. 6.

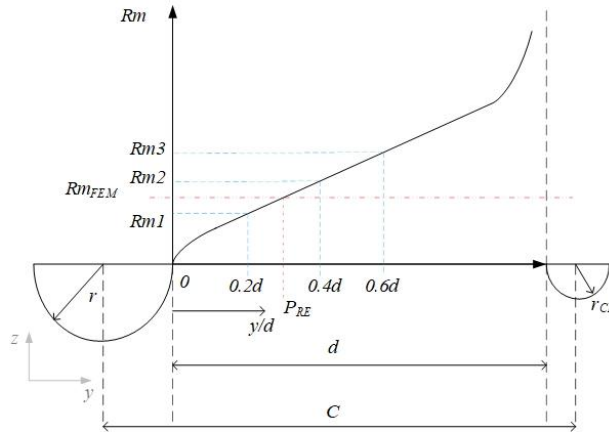


Fig. 6. Typical simulations result for data extraction and analysis.

For each scenario, the intersection between the measured  $R_m$  profile and the FEM-based reference  $R_{E,FEM}$  gives the normalized position  $P/d$ , while the slope  $\mu$  is computed from (5). These values are combined to obtain a general  $P/d$  function suitable for field use, replacing the original Tagg-based procedure in IEEE 81 [1, 3]. Because  $d$  coincides with the measurable zero-reference of  $R_m$ , it provides a more practical distance variable than  $C$ , as further discussed in the results section.

## 4. Results

### 4.1. Voltage profiles

Figure 8 shows the FEM-computed voltage profiles for hemispherical electrodes E and CE for several separation distances  $d$ . These profiles illustrate the influence of electrode proximity on potential-field superposition, a key factor affecting FoPM-based techniques and the 61.8% rule. Although Fig. 7b and Fig. 7c presents the case  $r = 100$  m and  $r_{CE} = 1$  m, the same qualitative behavior is observed for all values of  $r$ , both in the potential distribution and the resulting  $R_m$  curves.

As shown in Fig. 7a, the voltage profiles are extracted along the  $y$ -axis at  $x = 0$  and  $z = 0$ , from the edge of electrode E up to 1500 m, covering the full range of relevant separations  $d$ . Decreasing  $d$  increases the superposition area, while larger  $d$  values approach the ideal FoPM behaviour illustrated in Fig. 2. For each scenario, the correct potential-electrode PE location is obtained by intersecting the simulated profile with the theoretical resistance  $RE_t$ ; this intersection, normalized as  $y/d$ , provides the corresponding theoretical PE position.

### 4.2. Measured resistance ( $R_m$ ) profile behavior as a function of distance ( $d$ )

Once the potential profiles are obtained for each combination of  $r$ ,  $r_{CE}$ , and separation  $d$ , they are converted into the corresponding  $R_m$  profiles. Using the theoretical resistance  $RE_t$  for hemispherical electrodes in uniform soil (13), the intersection between  $R_m$  and  $RE_t$  yields the normalized position  $P/d$  at which the PE should be placed. Figures 8 and 9, summarize the behavior of  $P/d$  across the specific scenarios with  $r = 100$  m and  $r = 500$  m.

$$RE_t = \frac{\rho}{2\pi} \cdot \left(\frac{1}{r}\right). \quad (13)$$

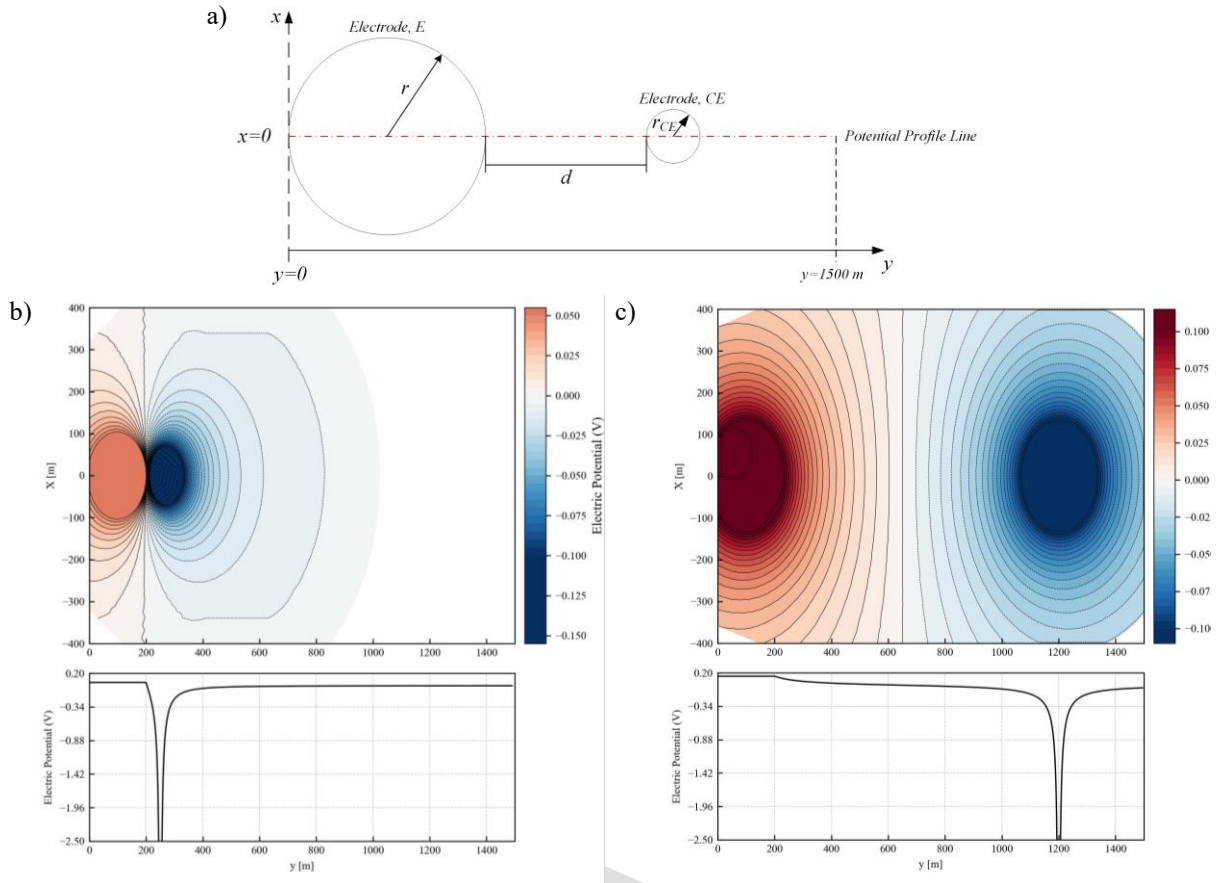


Fig. 7. Voltage profile. a) Geometrical description, b)  $d=50$  m, c)  $d=1500$  m.

The theoretical value of  $RE_t$  for the different studied scenarios is presented in Table 3.

Table 3. Evaluation of  $RE_t$  for various values of  $r$ .

$r$ [m]	100	200	300	500
$RE_t$ [ $\Omega$ ]	0.16	0.08	0.05	0.03

For large  $d$ , the intersection converges to the classical 61.8% position defined in the IEEE FoPM [1, 3], while for smaller  $d$  the optimal PE location progressively shifts toward electrode E.

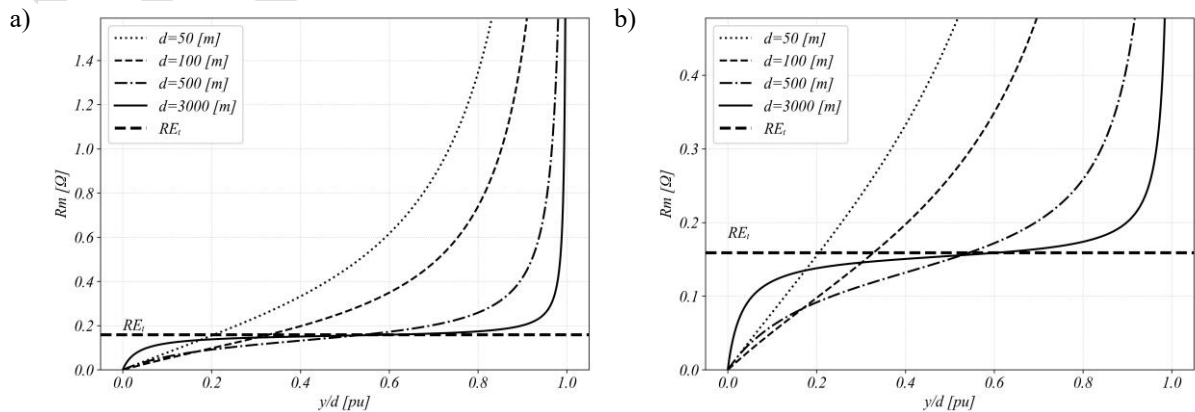


Fig. 8.  $R_m$  for  $r = 100$  m for various distances  $d$ : a) full potential profile, b) detail near theoretical resistance intersection.

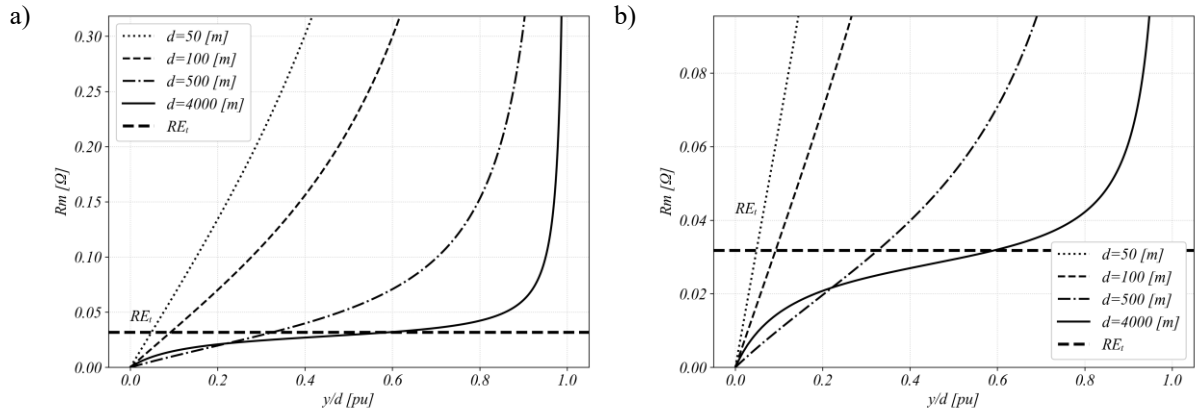


Fig. 9.  $R_m$  for  $r = 500$  m for various distances  $d$ : a) full potential profile, b) detail near theoretical resistance intersection.

### 4.3. Analysis of data for a functional relationship between Potential Electrode Position ( $P/d$ ) and slope ( $\mu$ )

Across all simulation scenarios, a consistent relationship is observed between the slope  $\mu$ , computed following Tagg [8] and IEEE procedures [1–3] using (5), and the normalized PE location  $P/d$ . For each FEM model,  $P/d$  is obtained from the intersection between the simulated  $R_m$  profile and the theoretical resistance, and the aggregated results are shown in Fig. 10 ( $P/d - FEM$ ). Figure 11 also compares these FEM data with the fitting expressions (6) and (9), revealing significant deviations reported in the literature for  $\mu > 1.4$ , which arise when  $d$  becomes very small. These discrepancies motivate the derivation of a new curve-fitted expression that improves the estimation of  $P/d$  and addresses the limitations noted in [10, 11, 13] and in the IEEE draft [3].

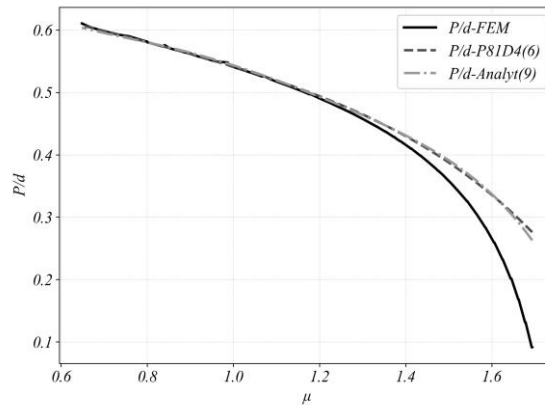


Fig. 10.  $P/d$  vs  $\mu$ .

Based on the  $\mu$  vs  $P/d$  dataset shown in Fig. 10, a fifth-order polynomial fit consistent with the IEEE formulation style was obtained, achieving a correlation of 0.9998. The resulting expression is given in

$$P/d = -3.4448 \cdot \mu^5 + 18.73 \cdot \mu^4 - 40.233 \cdot \mu^3 + 42.432 \cdot \mu^2 - 22.088 \cdot \mu + 5.149. \quad (14)$$

## 5. Application to Case Studies

### 5.1. Description of cases

A key goal of this work is to show that the corrected methodology can be reliably applied to large-scale grounding systems, including those found in renewable energy facilities. To demonstrate this, the following section applies the method to three representative case studies using FEM simulations, providing a detailed evaluation of its accuracy and its advantages over conventional measurement approaches:

- Case 1: A square grounding grid with a 500 m side,
- Case 2: A square grounding grid with a 1000 m side, and
- Case 3: A typical simplified grounding arrangement of a utility-scale photovoltaic plant.

In all three scenarios, electrode E is modeled as a 5-cm-radius copper conductor buried 2 m deep (Fig. 11a), and the current electrode CE as a 1-m-radius hemispherical electrode. All simulations assume uniform soil resistivity of  $100 \Omega \cdot m$ , a 1 A injected current, and remote boundaries at zero potential. For the square grids ( $L = 500$  m and 1000 m), two measurement profiles are considered—one originating from a corner and another from the midpoint of a side (Fig. 11b). The photovoltaic-plant model (Fig. 11c) consists of five 1000-m branches connected to a  $50 \times 100$  m substation mesh, with the profile taken from a substation corner. In every case, the voltage is obtained along a straight line from the selected point on E toward CE, converted into  $R_m$ , and compared with the theoretical resistance of each geometry, obtained from an additional FEM simulation using only the *ground-potential rise* (GPR). The resulting intersection provides the corresponding  $P/d$ , which is then evaluated against the corrected slope-method prediction given by (14).

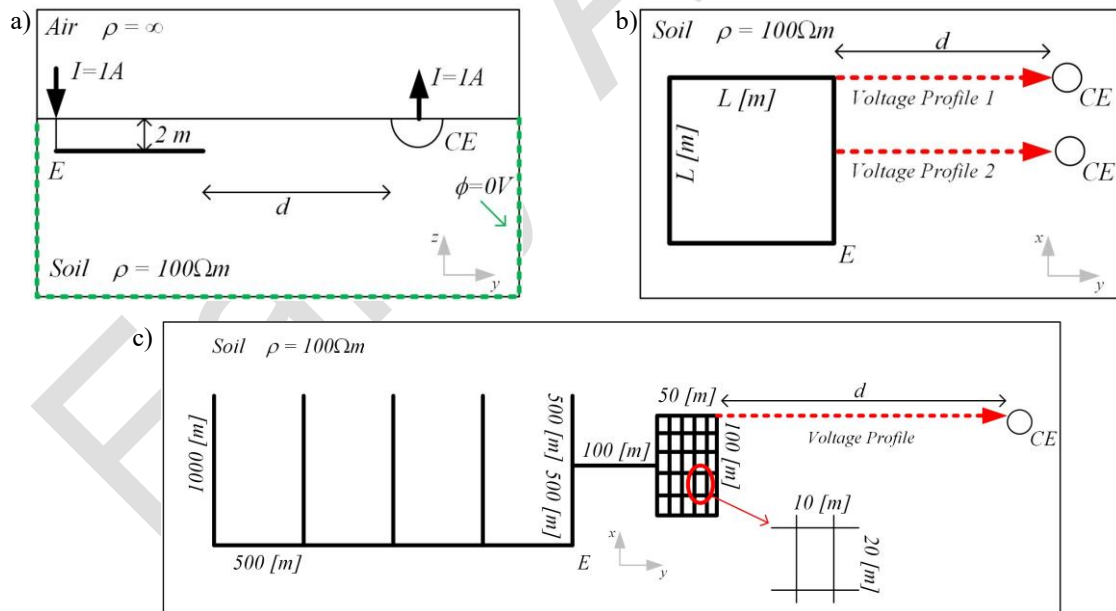


Fig.11. Geometry used for the studied cases: a) general characteristics of burial depth and soil conditions, b) schematic layout and voltage profiles for the square grid, and c) overall layout and voltage profiles for the photovoltaic plant.

### 5.2. Case 1: Results

For *Case 1*, corresponding to the  $500 \text{ m} \times 500 \text{ m}$  grid shown in Fig. 11, FEM-computed potential profiles were obtained for  $d = \{100, 250, 500, 1000, 1500, 3000\}$  m, as illustrated in

Fig. 12 for both measurement profiles. The difference between *Profile 1* (corner-based) and *Profile 2* (mid-side) is noticeable only for very small separations, mainly for  $\mu < 100$  m, which corresponds to  $d/DIAG < 0.14$  for this grid; this range is therefore excluded from the subsequent analysis (*DIAG* is the diagonal distance of the square mesh as illustrated in Fig. 13).

The reference resistance for this case,  $RE_t = 0.117 \Omega$ , was obtained from FEM. For each separation  $d$ , the intersection between  $R_m$  and  $RE_t$  provided  $P/d_t$ , while the slope  $\mu$  was computed from (5) and used to estimate the expected PE position using both the IEEE formulation [3] and the FEM-based expression. The predicted positions were mapped onto the corresponding  $R_m$  curves to determine the estimated resistances, and the errors were evaluated using:

$$\text{Error (\%)} = \left| \frac{RE_m - RE_t}{RE_t} \right| \cdot 100. \quad (15)$$

Tables 4 and 5 show that the IEEE method exhibits large errors when  $\mu > 1.4$ , whereas both formulations perform similarly for  $0.6 < \mu < 1.4$ , consistent with the  $\mu$ - $d$  trend in Fig. 12. They also highlight the effect of the measurement path: corner-based measurements (*Profile 1*) are more sensitive to distortion at small  $d$ , yielding average errors near 5%, while mid-side measurements (*Profile 2*) keep errors below 2.5%. Finally, the corrected TSM provides reliable estimates even for  $d/DIAG \approx 0.2$ , as shown in Fig. 13, enabling practical reduced-distance measurements with the CE placed near the grid boundary.

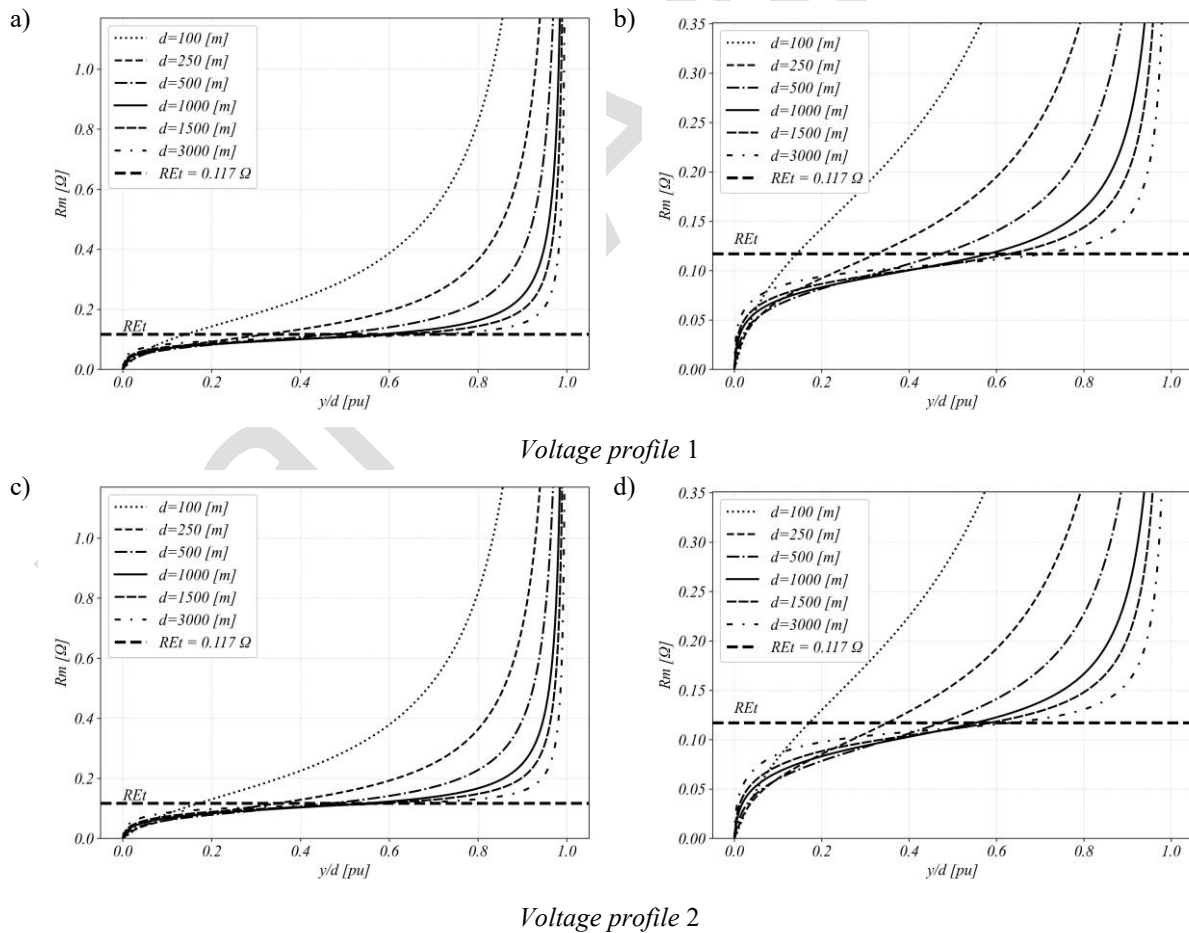


Fig.12.  $R_m$  (Case 1) a), c) full fall of potential profile, b), d) detail near theoretical resistance intersection.

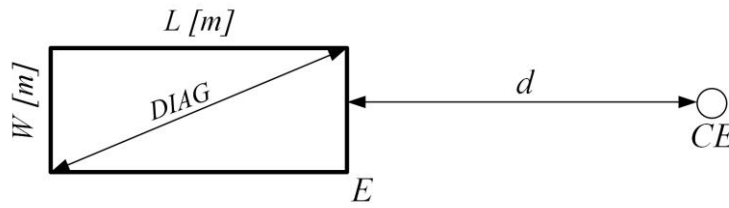


Fig. 13. Visualization of  $d/DIAG$  concept for an equivalent rectangular grounding system.

In conclusion, this case study demonstrates that the proposed methodology is a valid and practical alternative, offering clear advantages over traditional methods under the conditions analyzed.

Table 4. Results for the studied case # 1 (*Voltage Profile 1*).

$d$ [m]	$d/DIAG$	$\mu$	$P/d_t$	$P/d$ (IEEE)	$RE_m$ (IEEE)	$P/d$ (FEM)	$RE_m$ (FEM)	Error [%] (IEEE)	Error [%] (FEM)
100	0.141	1.667	0.143	0.294	0.185	0.118	0.105	57.89	10.16
250	0.354	1.523	0.327	0.377	0.128	0.321	0.116	9.55	0.50
500	0.707	1.335	0.477	0.453	0.114	0.431	0.111	2.48	5.11
1000	1.414	1.099	0.587	0.519	0.111	0.515	0.110	5.51	5.88
1500	2.121	0.963	0.636	0.549	0.110	0.551	0.110	5.66	5.57
300	0.424	0.780	0.714	0.584	0.111	0.581	0.110	5.55	5.68

Table 5. Results for the studied case # 1 (*Voltage Profile 2*).

$d$ [m]	$d/DIAG$	$\mu$	$P/d_t$	$P/d$ (IEEE)	$RE_m$ (IEEE)	$P/d$ (FEM)	$RE_m$ (FEM)	Error [%] (IEEE)	Error [%] (FEM)
100	0.141	1.642	0.171	0.310	0.181	0.166	0.115	54.61	1.49
150	0.212	1.588	0.244	0.343	0.149	0.250	0.119	27.54	2.13
200	0.283	1.534	0.305	0.371	0.135	0.310	0.119	15.40	1.70
250	0.354	1.482	0.352	0.396	0.128	0.353	0.118	9.15	0.79
500	0.707	1.258	0.476	0.477	0.118	0.461	0.115	0.77	1.45
1000	1.414	1.003	0.557	0.541	0.116	0.541	0.116	0.94	0.89
1500	2.121	0.883	0.592	0.565	0.115	0.565	0.115	1.33	1.30
3000	4.243	0.743	0.644	0.591	0.115	0.587	0.115	1.65	1.79

### 5.3. Case 2: Results

For Case 2, corresponding to a square geometry with  $L = 1000$  m sides ( $DIAG = 1414$  m), the obtained potential profiles are presented in Fig. 14 for the following values of  $d = \{250, 500, 1000, 1500, 3000\}$  m. For this geometry, the resistance value  $RE_t$  corresponds to  $0.0637 \Omega$ .

Table 6 summarizes the results for Case 2, where the analysis uses the profile that produces the largest errors. As the grounding-system size increases (larger  $DIAG$ ), a given  $d/DIAG > 0.14$  corresponds to larger absolute distances, placing the measurement point farther from the corner and reducing distortion. Consequently, errors are lower than in Case 1: the maximum remains below 7%, and in most cases stays under 2%.

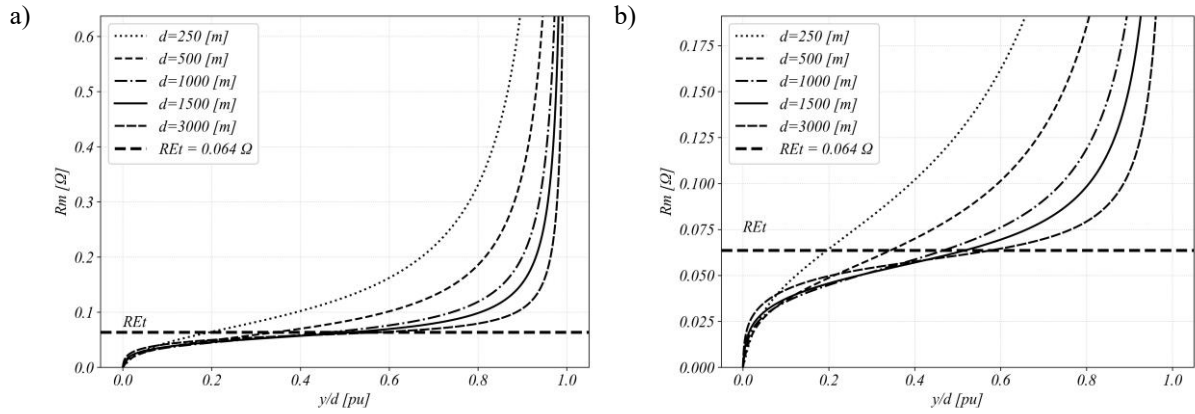


Fig. 14.  $R_m$  (Case 2): a) full fall of potential profile, b) detail near theoretical resistance intersection.

Table 6. Results for the studied case # 2.

$d$ [m]	$d/DIAG$	$\mu$	$P/d_t$	$P/d$ (IEEE)	$RE_m$ (IEEE)	$P/d$ (FEM)	$RE_m$ (FEM)	Error [%] (IEEE)	Error [%] (FEM)
250	0.177	1.610	0.195	0.330	0.088	0.220	0.068	38.19	6.77
500	0.354	1.480	0.344	0.397	0.070	0.355	0.065	9.38	1.89
1000	0.707	1.256	0.468	0.478	0.065	0.462	0.063	1.26	0.76
1500	1.061	1.103	0.518	0.518	0.064	0.513	0.063	0.03	0.44
3000	2.121	0.881	0.579	0.565	0.063	0.566	0.063	0.81	0.79

#### 5.4. Case 3: Results

This case study models a simplified grounding system for a 25–30 MWp PV plant. As shown in Fig. 11, the system comprises five 1000-m branches spaced 500 m apart, connected to a 50 m × 100 m substation grid with a 10 × 20 m mesh (total equivalent  $DIAG \approx 2300$  m). Copper conductors of 10 cm diameter are buried 1 m deep, and FEM analysis yields a theoretical grounding resistance of  $RE_t = 0.01770 \Omega$ .

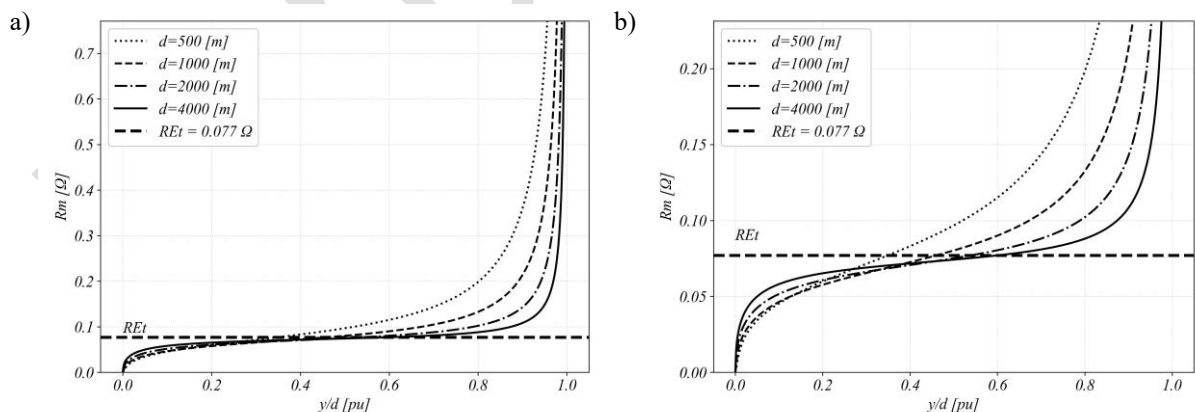


Fig. 15.  $R_m$  (Case 3) for various distances  $d$ : a) full fall of potential profile, b) detail near theoretical resistance intersection.

In Figure 15, the measured resistance profiles  $R_m$  are shown for different values of  $d$ , while Table 7 summarizes the main outcomes derived from applying the methodology. It can be observed that, for  $d$  values on the order of 500 m (approximately 0.25 of the system diagonal

(DIAG)), the corrected methodology already provides an accurate estimation of the grounding resistance of the evaluated system.

Table 7. Results for the studied case # 3.

$d$ [m]	$d/DIAG$	$\mu$	$P/d_r$	$P/d$ (IEEE)	$RE_m$ (IEEE)	$P/d$ (FEM)	$RE_m$ (FEM)	Error [%] (IEEE)	Error [%] (FEM)
500	0.215	1.377	0.349	0.439	0.088	0.413	0.085	14.41	10.16
1000	0.429	1.173	0.461	0.501	0.080	0.491	0.080	4.34	3.25
2000	0.858	0.976	0.541	0.546	0.077	0.548	0.077	0.49	0.58
4000	1.717	0.819	0.603	0.577	0.076	0.575	0.076	0.91	0.99

In summary, three study cases have been evaluated (from FEM simulations) to demonstrate the technical feasibility of the proposed methodology, thereby justifying the update of the expression used to determine the position of the potential electrode as a function of  $\mu$ .

## 6. Conclusions

Finite element simulations demonstrate that the traditional Tagg Slope Method introduces significant errors when the auxiliary electrode is placed at reduced distances. Two sources dominate these errors: neglecting finite electrode dimensions and using correction curves outside their original validity range. The corrected relationship derived in this work reproduces numerical results with a maximum fitting deviation below 0.02%.

Application to three large grounding systems (500 m square grid, 1000 m square grid, and a photovoltaic-plant grounding system) shows that, when measurements avoid corner regions and the auxiliary electrode is located at distances greater than approximately 20% of the system diagonal, the corrected method estimates grounding resistance with typical errors below 3%. For the same conditions, the traditional formulation produces errors ranging from about 10% up to more than 50% when the slope parameter ( $\mu$ ) exceeds 1.4.

For measurements taken near corner regions, errors increase for both methodologies. In these cases, average errors remain below 5% using the corrected formulation but can exceed 25% with the traditional approach when the auxiliary electrode is placed too close to the grounding system.

The results confirm that the revised formulation extends the reliable use of reduced-distance measurements to very large grounding systems, allowing practical measurements with auxiliary-electrode distances on the order of 20% of the system diagonal instead of the several times diagonal distance typically required by conventional fall of potential methods.

## Acknowledgements

I gratefully acknowledge the High Voltage Laboratory at Simón Bolívar University, Caracas, Venezuela, for providing the opportunity to conduct extensive grounding system tests over 20 years. Special thanks to Professors Jorge Ramírez, Juan Carlos Rodríguez, and Technician Ismael Acosta for their invaluable support.

## References

- [1] IEEE Guide for Measuring Earth Resistivity, Ground Impedance, and Earth Surface Potentials of a Grounding System. (2012). *IEEE Std 81-2012 (Revision of IEEE Std 81-1983)*, 1–86. <https://doi.org/10.1109/ieeestd.2012.6392181>

- [2] IEEE Guide for Measurement of Impedance and Safety Characteristics of Large, Extended or Interconnected Grounding Systems. (1991). *IEEE Std 81.2-1991*, 1–112. <https://doi.org/10.1109/iecestd.1992.106970>
- [3] IEEE Approved Draft Guide for Measuring Earth Resistivity, Ground Impedance, and Earth Surface Potentials of a Grounding System. (2025). *IEEE P81/D4, January 2025*, 1–170. <https://ieeexplore.ieee.org/document/10945631>
- [4] Martínez, M. (2014). Methodology based on neural networks for earth resistivity interpretation in congested urban areas. *Ingeniería Energética*, 35(1), 59–69. <http://scielo.sld.cu/pdf/rie/v35n1/rie07114.pdf>
- [5] Huang, H., Liu, H., Luo, H., Du, H., Xing, Y., Li, Y., Dawalibi, F. P., Zhou, H., & Fu, L. (2013). Analysis of a large grounding system and subsequent field test validation using the fall of potential method. *Energy and Power Engineering*, 05(04), 1266–1272. <https://doi.org/10.4236/epe.2013.54b240>
- [6] Leal, A. G., Lazzaretti, A. E., & López-Salamanca, H. L. (2022). A systematic review on grounding impedance measurement in electrical installations. *Electric Power Systems Research*, 214, 108953. <https://doi.org/10.1016/j.epr.2022.108953>
- [7] Tagg, G. F. (1964). *Earth resistances*. The Whitefriars Press Ltd.
- [8] Tagg, G. (1969). Measurement of the resistance of an earth-electrode system covering a large area. *Proceedings of the Institution of Electrical Engineers*, 116(3), 475. <https://doi.org/10.1049/piee.1969.0097>
- [9] Corbellini, G., & Corbellini, U. (1995). Definition and measurement of the earth resistance of an electrode covering a large area. *European Transactions on Electrical Power*, 5(3), 173–180. <https://doi.org/10.1002/etep.4450050305>
- [10] Raizer, A., Valente, W., & Coelho, V. L. (2017). Development of a new methodology for measurements of earth resistance, touch and step voltages within urban substations. *Electric Power Systems Research*, 153, 111–118. <https://doi.org/10.1016/j.epr.2017.01.025>
- [11] Raizer, A., Coelho, V. L., Valente, W., & Cardoso, C. I. (2015). Contribution to TAGG's methodology in the resistance measurement of earth-electrode systems at reduced distances. In *2015 International Symposium on Lightning Protection (XIII SIPDA)* (pp. 109–115). <https://doi.org/10.1109/sipda.2015.7339307>
- [12] Alcantara, F. R. (2018). An approximated procedure to find the correct measurement point in the Fall-of-Potential method. In *IEEE PES Transmission & Distribution Conference and Exhibition - Latin America (T&D-LA)* (pp. 1–5). <https://doi.org/10.1109/tdc-la.2018.8511738>
- [13] Moreno, J., Simón, P., Faleiro, E., García, D., Denche, G., & Asensio, G. (2024). A simple procedure to obtain the grounding resistance measurement of very large and urban electrodes by a modified Fall-of-Potential method. *Applied Sciences*, 14(17), 8040. <https://doi.org/10.3390/app14178040>
- [14] Berberović, S., & Boras, V. (2000). Correction of resistance measurement of large grounding systems. *European Transactions on Electrical Power*, 10(2), 105–111. <https://doi.org/10.1002/etep.4450100207>
- [15] Sunjerga, A., Rachidi, F., Rubinstein, M., & Poljak, D. (2018). Calculation of the grounding resistance of structures located on elevated terrain. *IEEE Transactions on Electromagnetic Compatibility*, 61(6), 1891–1895. <https://doi.org/10.1109/temc.2018.2877214>
- [16] Sunjerga, A., Rubinstein, M., Poljak, D., Karami, H., & Rachidi, F. (2020). Grounding resistance of a hemispheric electrode located on the top of a Finite-Height, Cone-Shaped mountain. *IEEE Transactions on Electromagnetic Compatibility*, 62(5), 1889–1892. <https://doi.org/10.1109/temc.2020.2974579>
- [17] Omar, R., Rani, M. A., Yunus, M. A., Isa, A. a. M., Mirza, W. I. W. I., Zin, M. S. M., & Roslan, L. (2018). Investigation of Mesh Size Effect on Dynamic Behaviour of an Assembled Structure with Bolted Joints using Finite Element Method. *International Journal of Automotive and Mechanical Engineering*, 15(3), 5695–5708. <https://doi.org/10.15282/ijame.15.3.2018.22.0437>
- [18] Silvester, P. P., & Ferrari, R. L. (1996). Finite elements for electrical engineers. In *Cambridge University Press eBooks*. <https://doi.org/10.1017/cbo9781139170611>
- [19] Sorgente, T., Vicini, F., Berrone, S., Biasotti, S., Manzini, G., & Spagnuolo, M. (2024). Mesh optimization for the virtual element method: How small can an agglomerated mesh become? *Journal of Computational Physics*, 521, 1–20. <https://doi.org/10.1016/j.jcp.2024.113552>
- [20] Megger. (2021). *Getting Down to Earth: A practical guide to earth resistance testin*. [https://www.megger.com/sites/g/files/utfabz201/files/acquiadam\\_assets/2021-04/GDTE\\_en.pdf](https://www.megger.com/sites/g/files/utfabz201/files/acquiadam_assets/2021-04/GDTE_en.pdf)



**Miguel Martínez Lozano** holds B.Sc. and M.Sc. degrees in electrical engineering from Simón Bolívar University (Venezuela) and a Ph.D. from the Technical University of Madrid (Spain). He has held academic and research positions at Simón Bolívar University and De La Salle Bajío University. He is currently a Lecturer at the Technical University of Madrid. His research focuses on electromagnetic

transients, insulation coordination, high voltage engineering, and dielectric behavior.

Early Access